

Development of a goniometric light scatter instrument with sample imaging ability

Myriam Zerrad*, Michel Lequime, Carole Deumié and Claude Amra

Institut FRESNEL, UMR CNRS 6133
Université Paul Cézanne - Ecole Centrale Marseille
Domaine Universitaire de Saint-Jérôme
13397 Marseille Cedex 20 (France)

ABSTRACT

The principle of a new scattering measurement system including a mobile lighting and a fixed CCD array is described. This new system allows a spatially resolved light scattering characterization. Moreover it is possible to separate localized defects contribution from the local roughness measurement. The comprehensive characterization of optical coatings can be performed with this set-up, and some examples will be given.

Keywords: light scattering, CCD, surface roughness

1. INTRODUCTION

The recording of the Bidirectional Reflectance Distribution Function (BRDF) of optical coatings deposited at the surface of plane substrates is widely used to quantify the amount of losses induced by scattering phenomena into the stack but also to identify these losses origin (interfaces roughness, layers volume defects) [1-5].

This measurement requires illuminating the sample with a laser beam at fixed incidence and recording the angular distribution of the scattered light intensity with a detector mounted on a rotating arm [6-10]. If this recording is achieved with a lighting beam whose diameter is comparable to the sample one, the presence of dust or localized scratches on the piece surface could alter the deduced roughness information. On the other hand, if the probe beam is tight focused, a 2D scan is necessary to achieve the complete surface characterization which leads to quite huge acquisition time.

To overcome this difficulty, we developed a new experimental set-up [11, 12] whose detection arm is fixed at zero degree-incidence while the lighting arm becomes mobile around the sample. The detection system is a back illuminated scientific grade CCD which allows imaging the optical surface, sampling it by about one million of elementary pixels, reaching ultra low BRDF levels and recording the diffraction pattern of any defect on the sample.

This CCD-ARS instrument already provided comprehensive information on surface defects as well as measuring the correct intrinsic roughness, but this method should still be improved and its range of application extended.

In this communication, we will perform a quick presentation method and a detailed description of this new improved set-up and we will provide some examples of applications especially for the comprehensive characterization of low roughness surfaces (pixelized BRDF measurements with localization and size estimation of defects).

2. NUMERICAL ANALISYS

In this section, we will briefly present a few numerical results illustrating our thought process and demonstrating all the interest of such a characterization method.

*myriam.zerrad@fresnel.fr; phone +33 4 91 28 87 16; <http://www.fresnel.fr/map2/diffusion/diffusion.php>

Our aim is not to develop here the exact procedure we used for our numerical simulations, first, because, it already has been detailed in previous publications [11], and then, because we prefer here focus our attention on the experimental set-up improvement. But, we think this step is necessary to understand the necessity of developing and improving such an experimental set up.

2.1 Impact of localized defects

Let us consider a low roughness plane silica surface shaped as a square (with side $L=500\mu\text{m}$) and illuminated by a collimated beam at wavelength $\lambda = 847 \text{ nm}$ in the air. These parameters have been chosen to well fit the experimental conditions of a standard light scattering measurement.

The surface profile is numerically generated to simulate a realistic surface and is expressed as an $N \times N$ matrix represented Fig. 1, with $N = 2L / \lambda$. Such a resolution ensures us the numerical simulations take care with surface variations in a spatial frequency range corresponding to the illumination wavelength.

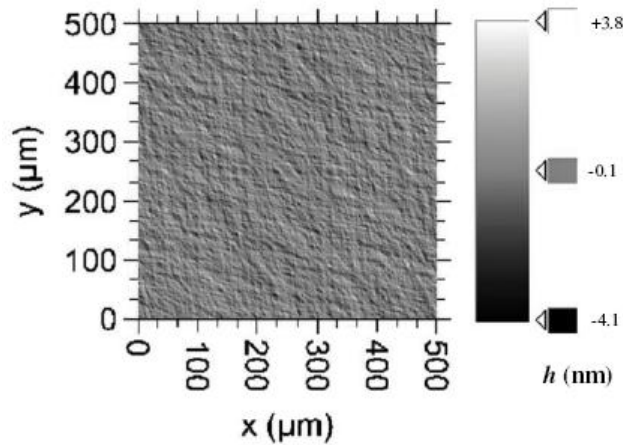


Fig. 1: Synthetic low-roughness surface model

On Fig. 2, we can see the BRDF calculated from the surface profile given Fig. 1 as a function of the scattering angle θ , in the incidence plane.

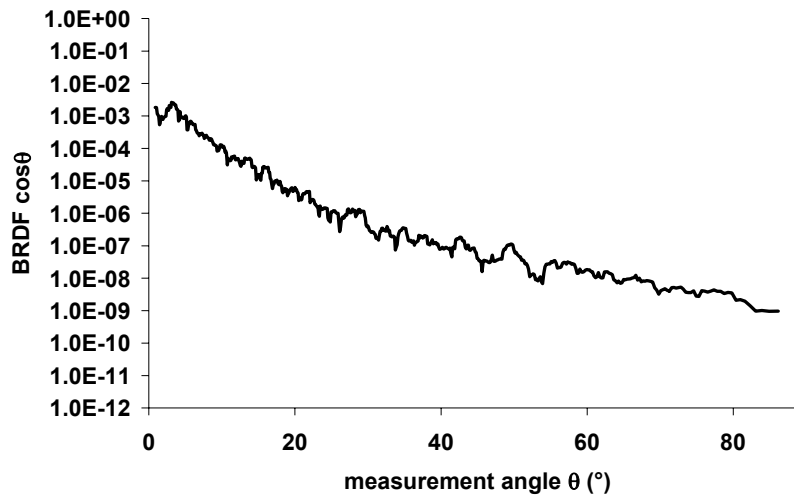


Fig. 2: BRDF calculated with first order theory from the surface profile given Fig. 1

The rms roughness δ of the sample in the spatial range $\left[0, \frac{2\pi n_0}{\lambda}\right]$ can be deduced from the classical [13] relationship (1)

$$\delta^2 = \int_{\sigma} 2\pi\sigma\gamma(\sigma)d\sigma \quad (1)$$

where γ is the roughness spectrum of the surface and can be computed from the BRDF in the incidence plane by the relationship

$$BRDF \cos \theta = C(\theta)\gamma(\theta) \quad (2)$$

where $C(\theta)$ is a term derived from electromagnetic theory [4, 5, 14] and θ , the measurement angle.

For the synthetic surface given Fig. 1, the relation ship (1) gives a rms roughness of 0.865 nm.

Let us numerically add to this surface some isolated dome shaped defects with random diameters between 3 and 8 μm and height less than 0.2 μm and whose refractive index is the same as the surface. The BRDF and, as a consequence, the rms roughness of the resulting surfaces will be affected.

As an illustration, you can see Fig. 3, the surface defined Fig. 1 with 10 localized defects and the corresponding BRDF whose level is obviously increased by the presence of these defects.

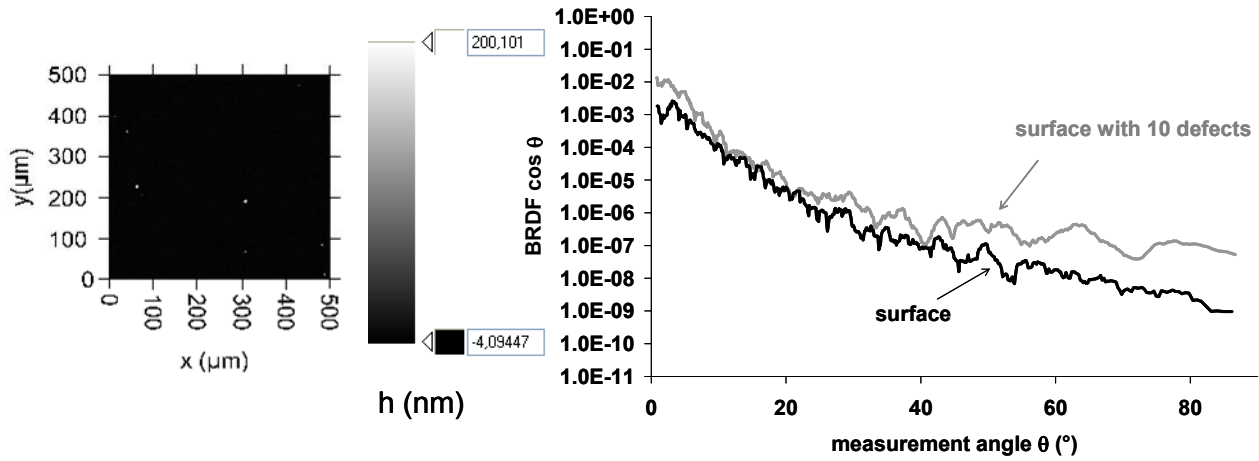


Fig. 3 : Influence of 10 localized dome shaped defects (with diameter between 3 and 8 μm and height less than 0.2 μm) on light scattering from a 500 μm x 500 μm^2 surface

Moreover, we can see Fig. 4 how the rms roughness is modified by adding different number of defects on the sample surface.

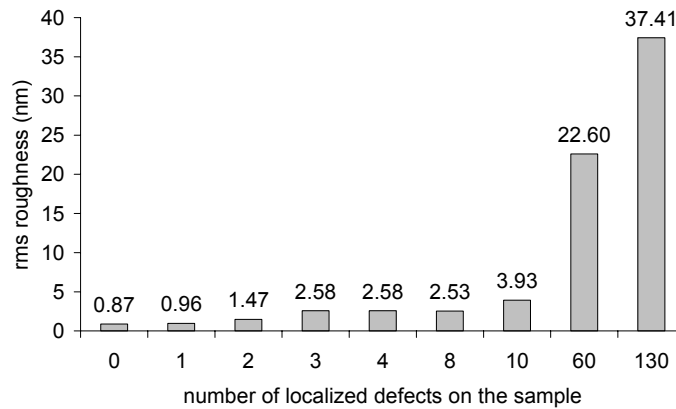


Fig. 4: rms roughness of the surface defined Fig. 1 with different numbers of isolated defects (with random diameter between 3 and 8 μm and height less than 0.2 μm)

Furthermore, we can see here that the presence of defects on the sample surface will perturb the scattering measurement on a significant way, even if the number of localized defects seems not to be significant. For example, 3 defects localized on the substrate will make the measured roughness nearly 3 times higher than the intrinsic roughness of the sample. This quotient increases with the number of defects in presence.

These numerical results are showing us the determination of the rms roughness of a surface through a scattered intensity measurement can very quickly become inaccurate because of the presence of a few localized defects on the surface.

As it is obviously impossible to take off every defect from the sample, the only way for us to reduce the probability to find a defect on the analyzed area is to reduce the dimensions of this analyzed area.

2.2 Analyzed area reduction

To reduce the analyzed area, we divide the synthetic surface into smaller squares, each with a surface area 100 times smaller (i.e. $50 \times 50 \mu\text{m}^2$). It is done Fig. 5 for the surface defined Fig. 3. The probability of having two defects in the analyzed area is greatly reduced, and may become negligible if the total number of defects remains small. Two different cases then have to be analyzed: either the surface element is free of defects (in which case the observed scattering function is representative of intrinsic roughness, for example, elementary surface A on Fig. 5 whose BRDF is given Fig. 6-a), or it includes only one defect. In the latter case, the scattering function will be greatly affected and instantly recognizable as it is shown Fig. 6-b for elementary surface B.

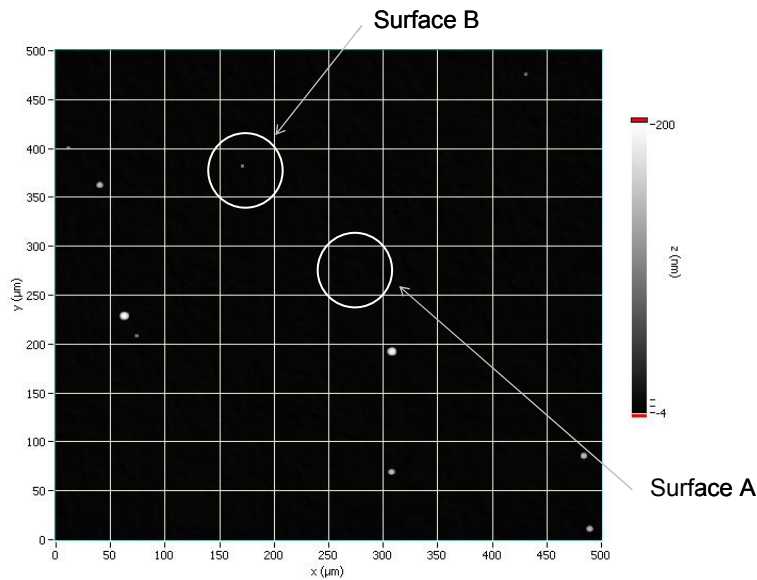


Fig. 5: Synthetic low-roughness surface with 10 defects defined Fig. 3 divided in 100 elementary $50 \times 50 \mu\text{m}^2$ surfaces

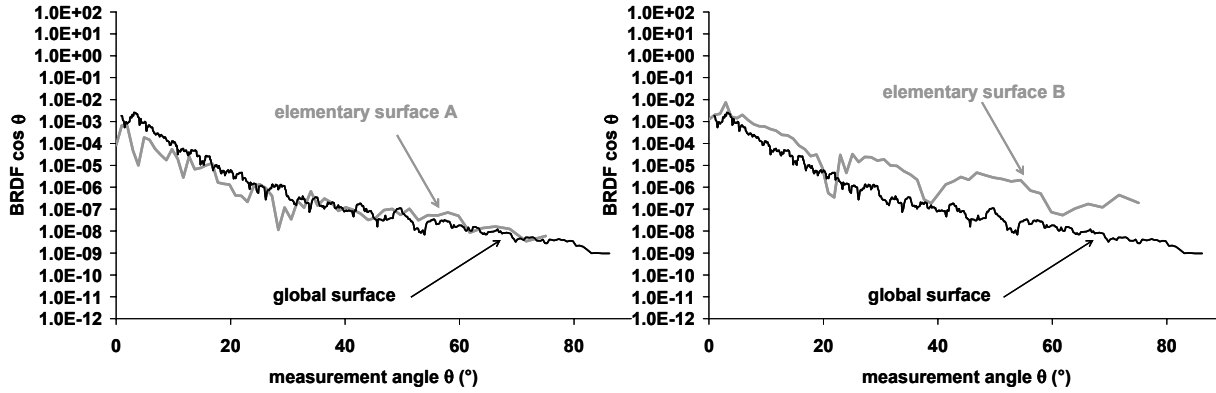


Fig. 6 a and b : BRDF of elementary $50 \times 50 \mu\text{m}^2$ surfaces A et B defined Fig. 5 compared with the BRDF of the full $500 \times 500 \mu\text{m}^2$ surface defect free defined Fig. 1. Surface A is chosen defect free and surface B contains one dome shaped defect.

If the elementary surface is defect free, the corresponding curve can be used to compute the rms roughness of the smaller region yields. For surface A, we obtain $\delta = 0.855 \text{ nm}$, which is very close to that determined for the whole surface in the same pulsation range, $\delta = 0.865 \text{ nm}$. On the other hand, the presence of a defect on the elementary surface is immediately identifiable by the presence of oscillations on the BRDF. In this case, the scattering function can closely be approximated by the Airy pattern corresponding to diffraction by the defect [15]. So that, lateral and axial dimensions of the defect can be deduced from the period and the amplitude of the oscillations. If the defect can be approximated by a circular stop of diameter $2a$, we can write:

$$BRDF \cos \theta \propto \left[\frac{J_1\left(\frac{2\pi a}{\lambda} \sin \theta\right)}{\frac{2\pi a}{\lambda} \sin \theta} \right]^2 \quad (3)$$

Moreover, in the case of a single defect with diameter greater than the diffraction limit (i.e., 1.22λ), the scattering function will present one or more oscillations. Its minima occurs at specific scattering angles θ_m given approximately by

$$\sin \theta_m \approx \frac{Z_m}{\pi} \frac{\lambda}{2a} \quad (4)$$

where the Z_m are zeros of the J_1 Bessel function (3.8317, 7.0156, 10.1735, and so on).

Now, the significance of reducing the dimensions of the analyzed area sounds as an obviousness. So, we have to define an optical set up allowing light scattering characterization of a whole sample dividing it in such a small surface.

To comprehensively characterize the roughness properties of a sample, we need to record the scattering function of each small surface element. If we consider a standard 1"-diameter optical substrate, for example, and wish to characterize at least 80% of its surface, then approximately $M = 160,000$ $50 \times 50 \mu\text{m}^2$ surface elements will need to be scanned. This number is quite large, especially if we keep in mind that each BRDF acquisition requires from 20 to 100 angular positions (\mathcal{A}).

To rapidly record so many data points ($M \times \mathcal{A}$ is about 10 millions) while maintaining a reasonable signal-to-noise ratio, some sort of multiplexed acquisition scheme is required. We chose to use spatial multiplexing by imaging the optical surface under testing in the focal plane of a CCD camera.

3. EXPERIMENTAL SET-UP

The use of a CCD spatial multiplexing scheme permits sampling of all surface coordinates simultaneously as long as we can guarantee stable relative positioning between the sample surface and the photodiodes of the array during the BRDF recording.

To guarantee this stability, we propose to fix the detection arm ($\theta=0$). The lighting arm becomes mobile instead, so that the incidence angle i can vary between a few degrees and 90 degrees. This choice leads to a new arrangement in which the position and orientation of the sample are constant relative to the detector. The sample is thus easily imaged on a CCD array. Moreover, we use a back-illuminated, scientific-grade CCD as the detector. This device samples about one million elementary pixels and is able to reach ultra-low BRDF levels thanks to the large integration time (up to 1 minute), enabled by the negligible dark current level.

Our first CCD-ARS set up already provided comprehensive information on surface defects as well as measuring the correct intrinsic roughness [11, 12], but its range of application should still be extended. In this aim, the set up has been improved to allow the extension of:

- The measurement angular range using a new lighting system
- The analyzed area dimensions and resolution using a new detection system
- The background level of parasitic light using a new sample holder

We will present now these last evolutions.

A schematic representation of the new CCD-ARS instrument is given in Fig. 7

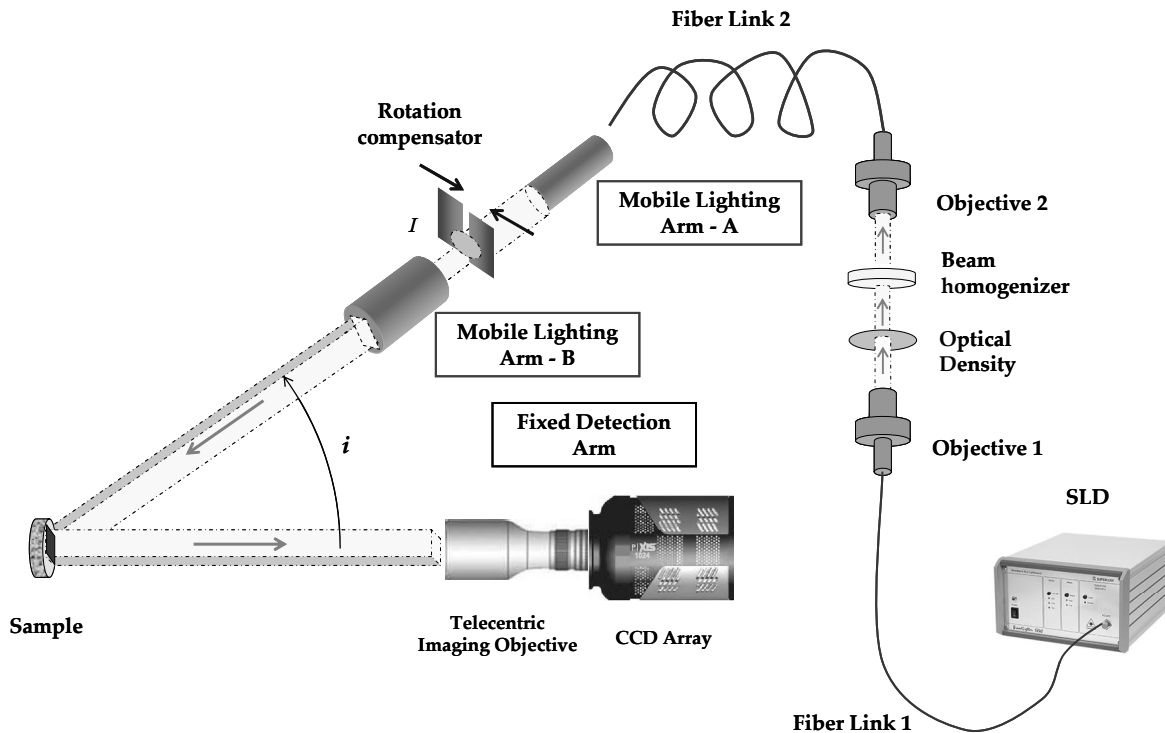


Fig. 7: the CCD ARS instrument

3.1 Lighting system

The light source is a high-power (15 mW) Super Luminescent Diode (SLD) centered at 840 nm, manufactured by Superlum[16]. Its spectral bandwidth ($\Delta\lambda=50$ nm) is large enough to cancel the far-field speckle typical of coherent laser lighting, yet quite similar to the monochromatic configuration assumed by our numerical simulations. The first fiber link

is a standard single-mode fiber (Corning Puremode HI-780), while the second is an all-silica, step index multimode fiber with core diameter $2a = 600 \mu\text{m}$ and numerical aperture $\sin \alpha = 0.25$. The two links are coupled via a pair of objectives. A beam homogenizer and a motorized wheel are installed between these 2 objectives, to uniform the lighting beam and adjust the light power with the help of an optical density (0, 1, 2 or 3).

A key point of this new set up lays in the conception of the lighting system. Before describing it, we have to remind that in the previous set up, the measurement of low scattering surfaces was limited to incidences angles from 20 to 60° . The illuminated area on the sample was an ellipse whose major axis is inversely proportional to $\cos i$, so that, for incidence angles higher than 63° , the area illuminated was larger than the sample diameter. Its effect on the background level can be troubling for low-roughness samples at incidence angles above 63° .

As in the previous set up, the lighting system is installed on a mechanical arm that rotates (by angle i) around the sample. (The axis of this rotation is vertical, and lies in the front face of the sample). This lighting arm is divided in two parts (part A and B on Fig. 7). Part A is a telecentric objective which will provide a magnified image I (the magnification is 10) of the multimode fiber's extremity which is located in its focal plane. Part B is an other telecentric objective which will image the intermediary image I on the sample surface with a magnification $M = 3.75$). So, of the illuminated area on the sample is a 22.5mm diameter disk.

To avoid the extension of the illuminated area during the scan, we added to the lighting arm a system to compensate the rotation effect on the spot by continuously morphing the beam. A rectangular diaphragm is positioned on the image focal plane of image I . By having variable dimensions, this diaphragm will allow us to have a constant 15.9 mm side square spot on the sample surface which is the dimension of the largest square which can be inserted in a 22.5 mm sample (we will explain in section 3.3 why the useful area on a 25 mm diameter sample is a 22.5 mm diameter circle).

The lighting arm rotates on the horizontal plane, so the vertical dimension of the diaphragm stays $15.9/M = 4.2$ mm during the whole scan. The horizontal aperture L of the diaphragm is defined as a function of the incidence angle i by the relationship:

$$L = \frac{15.9}{M} \cos i \quad (5)$$

By using such a rotation compensator, the shape of the illuminated region can be maintained identical during the angular scan and the scan range can be extended to 85° . For incidence angles higher than 85° , the side of the sample holder is hiding a part of the beam.

So, with the lighting system we designed, a 25mm diameter sample will be illuminated with incidence angles from 13 to 85° with a spot shaped as a 15.9 mm side square.

Let us now define the detection system.

3.2 Detection system

The surface of the sample is imaged by a Princeton Instruments PIXIS 1024B camera [17], which uses a back-illuminated, scientific-grade CCD with a 1024×1024 imaging array and 100% fill factor (square pixels, with side $p = 13 \mu\text{m}$). At the SLD's central wavelength, the quantum efficiency η of the CCD is about 60%. The camera can be maintained at -70°C by means of an interior thermoelectric cooler; at this temperature, the dark current is limited to $0.001 \text{ e}^-/\text{pixel}/\text{s}$. The single-pixel full well figure is around 120 ke^- . Read-out and digitization of the CCD data are performed at 100 kHz on 16 bits (read noise $4.3 \text{ e}^- \text{ rms}$).

The imaging objective is a custom telecentric lens from Light Works [18], with magnification $G = 0.5$, a working distance of 400 mm, and a nominal aperture number of 16 (N). We stress that the telecentric objective is a key element defining the characteristics of our instrument. In a telecentric objective the entrance pupil is rejected at infinity, which guarantees that the angular coordinates of the chief ray defining the direction of scattered light are the same at all points on the sample surface. This property is illustrated in Fig. 8.

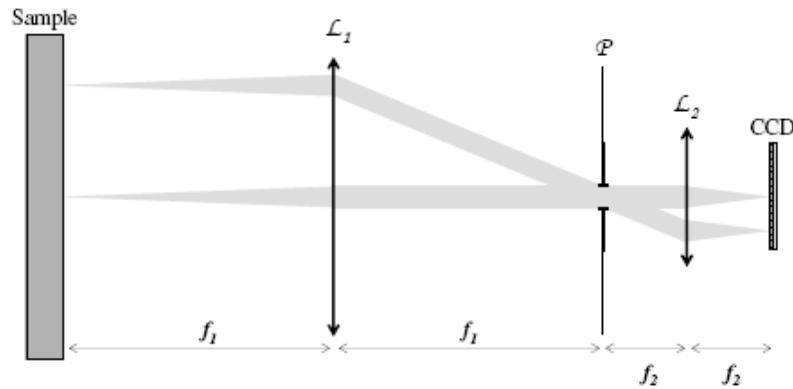


Fig. 8: The working principle of a telecentric objective used as an imaging device

An aperture stop is placed in the common focal plane of lenses \mathcal{L}_1 and \mathcal{L}_2 , which are used to simulate the telecentric objective. The entrance pupil and exit pupil are located at infinity, so the chief ray is horizontal in both sample space and CCD space for any pixel of the detector array. The field of view of the detector can be controlled by adjusting the diameter of the aperture stop. The magnification factor G is determined by the focal lengths of the two lenses ($G = f_2 / f_1$). The half-divergence α of a scattered beam entering the pupil of the imaging objective is about 0.89° ($\tan \alpha = G / 2N = 0.015$). Moreover, the area imaged by the CCD camera is $1024 \text{ p}/G = 26.62 \text{ mm square}$, so the whole sample can be imaged. As indicated previously this telecentric configuration is also implemented in the lighting system, which guarantees that the angular coordinates of the beam are identical for all points on the surface of the sample.

It is important to note here that the use of a high F-number telecentric objective coupled with a tightly collimated lighting beam is a key point of our set up. It is thanks to these two elements that our experiment provides accurate light scattering measurements instead of simple surface imaging.

3.3 Sample holder

Testing the previous CCD-ARS instrument, we realized our detection system is so sensitive that any element on the light trajectory can become a source of parasitic light and perturb the scattering measurement. So, to record the BRDF sample in optimal conditions, the scan would have to be performed with a sample holder perfectly invisible for the CCD-ARS set up. To approximate this objective, we designed a new sample holder whose visible surface is drastically reduced.

A schematic of this sample holder is given Fig. 9. It is a 25 mm diameter ring with a 1 mm thickness united with a second 1mm thick ring whose internal and external diameters are respectively 22.5 and 26mm. The sample is held by the first ring by pressure effect and blocked by the second ring. The whole sample holder is black anodized to limit the amount of possible stray light and it is linked by three threads to an external support which is far (more than 30 cm) from both the field of view of the detection system and the illuminated area. With such a sample support, the visible part of a 25 mm diameter sample is a 22,5 mm diameter circle.

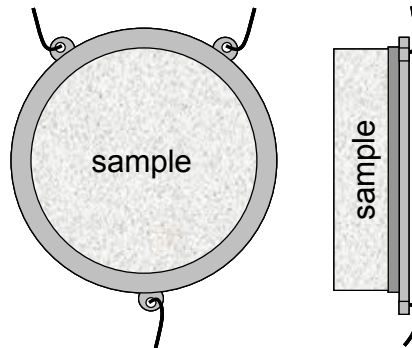


Fig. 9: sample holder, schematic front and side views

As an illustration of our measurement configuration, you can see Fig. 10 an image of a 25 mm diameter ZnSe sample illuminated with an incidence angle $i = 15^\circ$ by the square shaped beam defined section 3.1 and maintained by the sample holder described section 3.3. As it can be seen, the sample holder seems nearly invisible for the detection system.

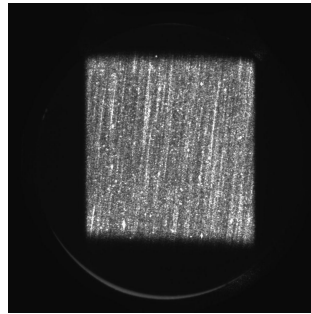


Fig. 10 : Image recorded with a ZnSe sample for a lighting angle of 13.5° and an integration time $\tau = 1.5$ s in our final measurement configuration

4. APPLICATIONS

4.1 Perfect diffuser

The characterization of a perfect diffuser is necessary to calibrate our CCD-ARS instrument. Figure 9 shows a sequence of images recorded by the CCD array for incidence angles between 13.5 and 90 degrees. As expected, the illuminated area keeps the same square shape.

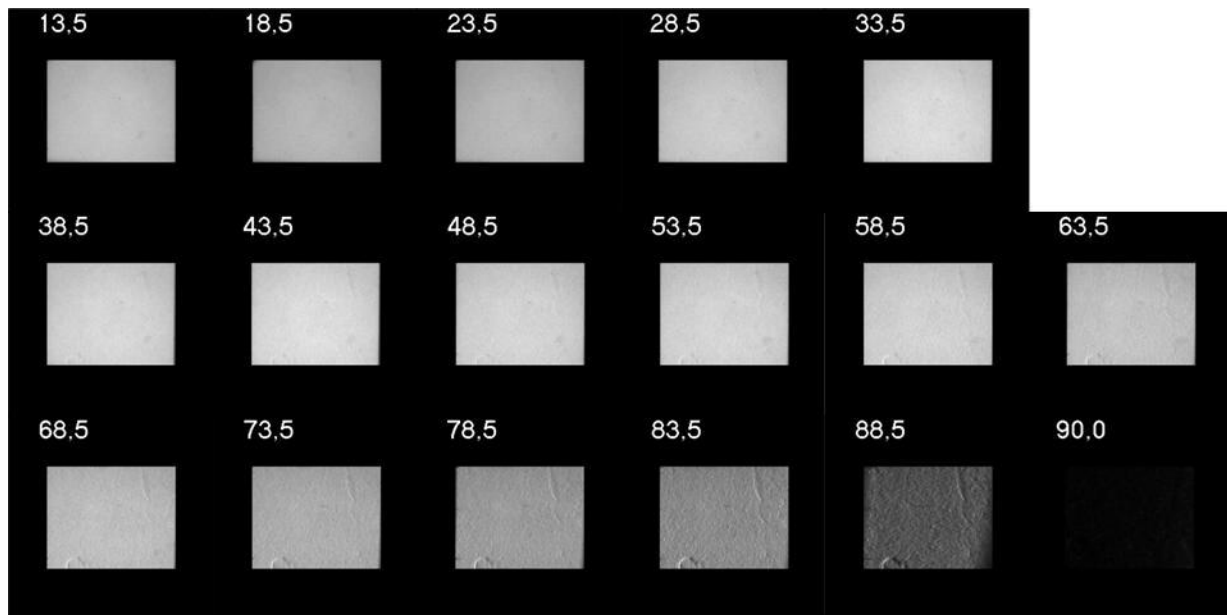


Fig. 11: CCD images recorded with a perfect diffuser.

The instrument can be calibrated for each pixel of the illuminated area. The angular response $G(i)$ is recorded for each pixel, and then it is fitted by the theoretical response of a perfect diffuser.

$$BRDF \cos i = \frac{1}{K} \frac{G(i)}{\tau} \cos i = \frac{\rho}{\pi} \cos i \quad (6)$$

where τ is the integration time and ρ the albedo of the perfect diffuser.

The calibration constant K was adjusted by a least-squares method for each pixel and allows the conversion from the image grey levels to the BRDF of the sample.

Fig. 12 shows the scattered light intensity recorded during this angular scan for one pixel, selected at random. The data are well fit by the theoretical response of a perfect diffuser. For all pixels inside the initially illuminated area, we obtain a similar level of agreement. This result confirms the validity of our measurement method.

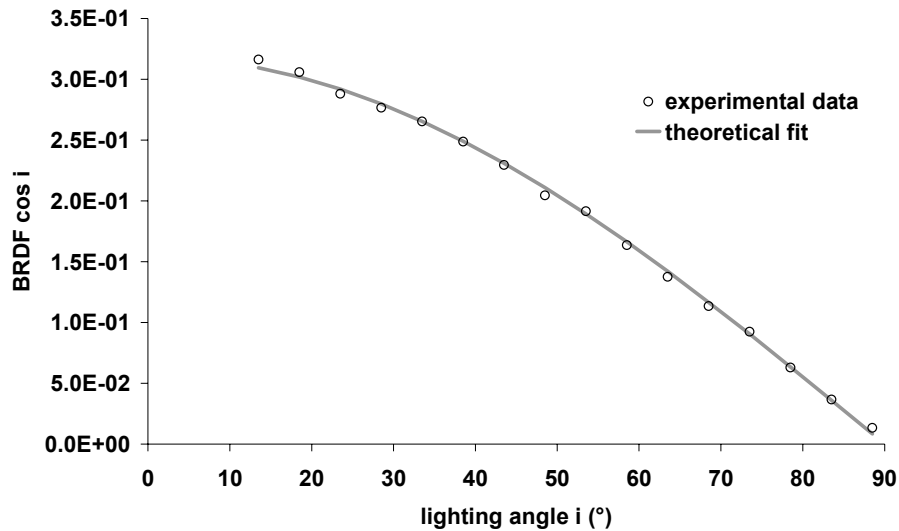


Fig. 12: angular response of a perfect diffuser. Experimental data

Figure 11 shows the values obtained for this calibration constant (K) for each CCD pixel inside a 13 mm square. The low frequency variations are due to the imperfect uniformity of the beam, but this effect can now be cancelled out across the whole image. High frequency variations are due to some imperfections on the surface of the diffuser.

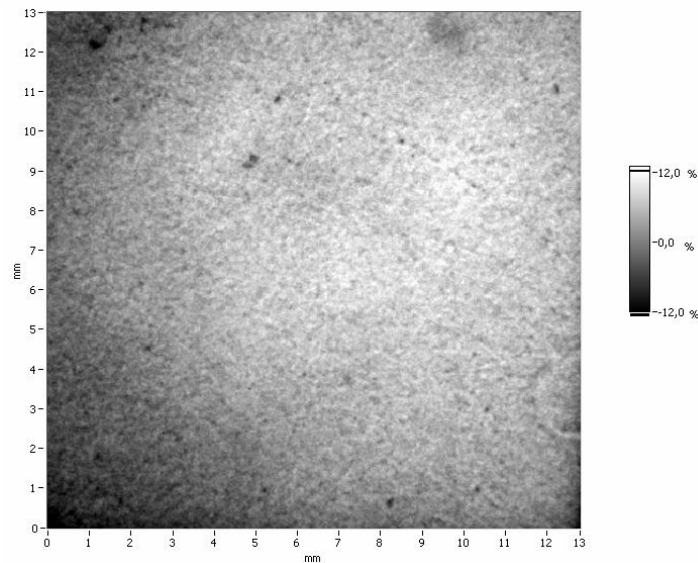


Fig. 13: Relative variation of the calibration constant K computed from a perfect diffuser scan at each pixel position within a 13 mm square

4.2 Instrument signature measurement

A signature measurement is the lowest level of BRDF measurable with a given Instrument. It is equivalent to the BRDF of an ideal, scatter-free sample due to instrument limitations. In our case, the signature was determined by removing the

sample and otherwise measuring the effective BRDF under the same conditions that would later be used in actual sample measurements. Accordingly, the incident angle varied between 13.5° and 90°, the optical density was set to zero, and the integration time was 200 seconds. The equivalent BRDF level varied from $7 \times 10^{-8} \text{ sr}^{-1}$ at 13.5° to $3 \times 10^{-8} \text{ sr}^{-1}$ at about 90°. The rms noise under these conditions is less than 10^{-9} sr^{-1} . The instrument signature is therefore dominated by stray light and Rayleigh scattering. Fig. 14 compares the result of this measurement to that achieved on a perfect diffuser.

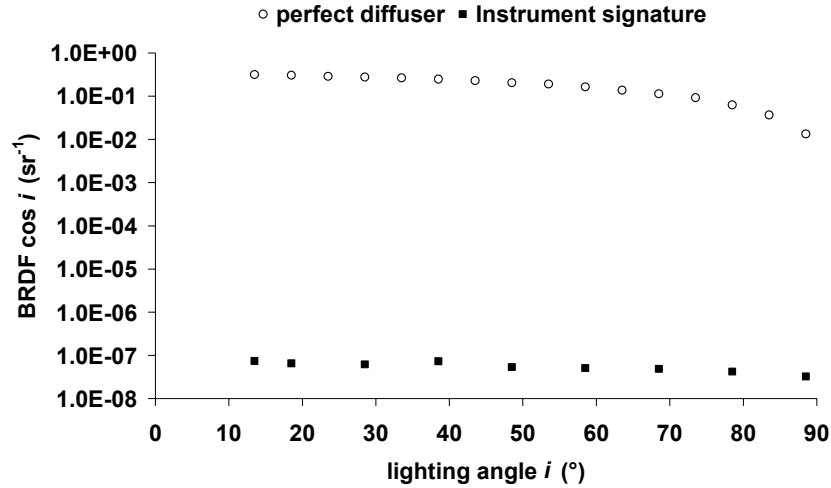


Fig. 14: CCD-ARS instrument signature for lighting angles between 13.5° and 88.5°. The scattering intensities of a perfect diffuser are plotted for comparison

4.3 Germanium wafer

To complete our evaluation of the CCD-ARS instrument and demonstrate its efficiency at locating isolated defects, we examine a low-roughness germanium wafer with some surface particles (due to imperfect cleaning or eventual polish scratches). The whole CCD image at a lighting angle of 13.5° is shown in Fig. 15. The intensity of the lighting beam is maximal (zero optical density) and the integration time is 20 seconds. In the saturated zones (solid white) excess photoelectrons flow over to surrounding pixels, usually in the same column. Obviously, the BRDF measurement can not be achieved in these regions of the CCD array.

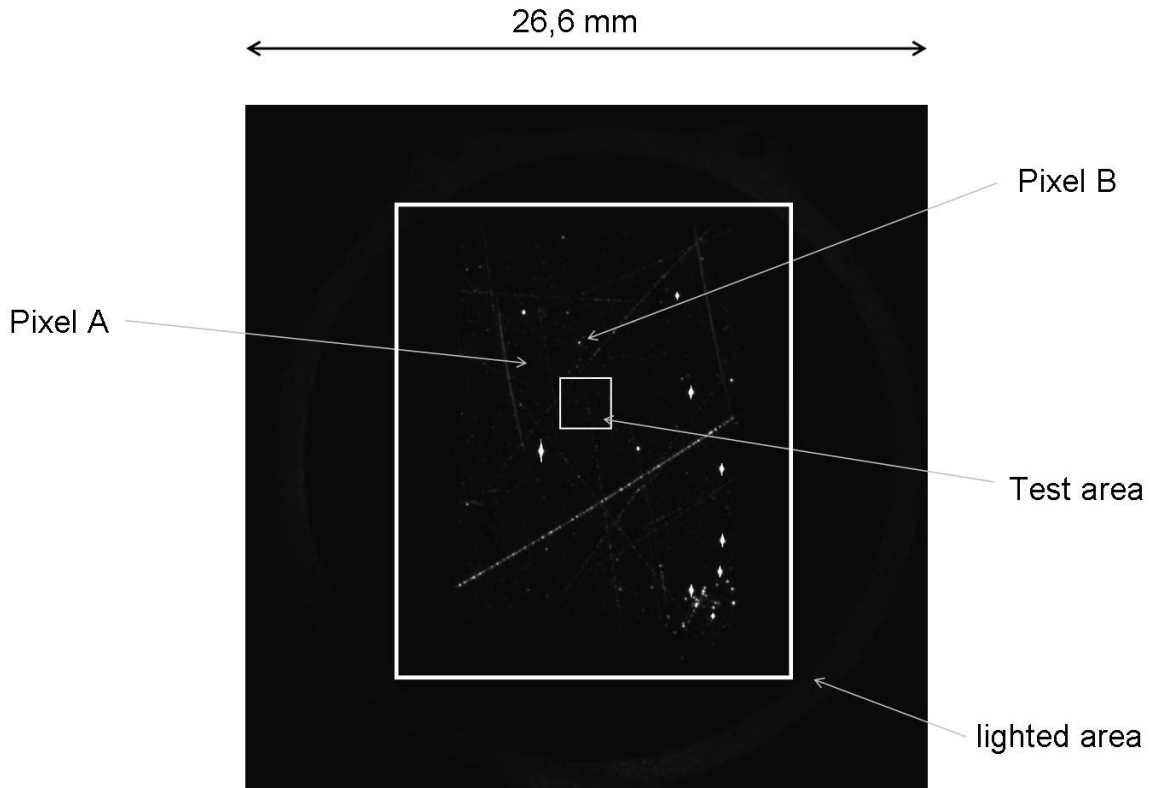


Fig. 15 : A germanium wafer imaged with the CCD-ARS instrument

The pixel labelled A on Fig. 15 is associated with a surface element which seems free of particles. The BRDF of this surface element, shown in Fig. 16, is a gradually decreasing function of angle. Its mean level is about 10^{-7} sr^{-1} , which is 5 times greater than the instrument signature. In contrast, the pixel labelled B on Fig. 15 is associated with a surface element which clearly contains a small and isolated defect.

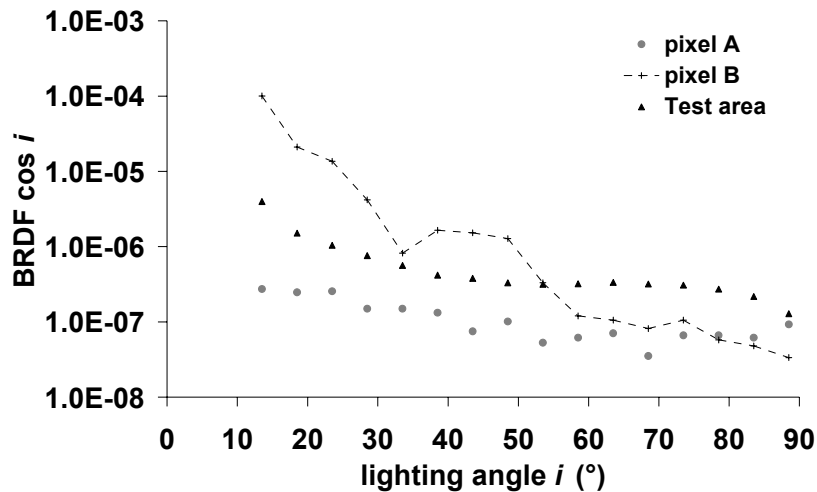


Fig. 16: Cosine-corrected BRDFs of selected pixels (pixel A: without a defect; Pixel B: with a single defect; Test area : a $2 \times 2 \text{ mm}^2$ square area)

The shape of the BRDF presents oscillations. It is clearly characteristic of diffraction from a small stop. The position of the minimum ($i_1 = 33.5^\circ$) indicates that the diameter $2a$ of this particle is about $1.8 \mu\text{m}$, since from (4) we can write:

$$2a \approx \frac{3.8317}{\pi} \frac{\lambda}{\sin i_1} \quad (7)$$

According to the same expression (4), the smallest particles which can be identified by this method will have a diameter of about $1 \mu\text{m}$. We note that each pixel of our camera is about $13 \mu\text{m}$ square, which means that the sample area observed by one CCD pixel is equal to $26 \mu\text{m}$ (the magnification of the telecentric objective is 0.5). These data therefore prove that our CCD-ARS instrument is capable of detecting extremely small structures, with lateral sizes thirty times smaller than the elementary area. This resolution is clearly an outstanding feature of our instrument.

Finally, we measured scattered light within a larger test area 2 mm square defined Fig. 15.

An enlarged view of this test area is shown in Fig. 17, to have a better visualisation of the surface defects, an inverted 16-bit logarithmic scale is chosen for the representation.

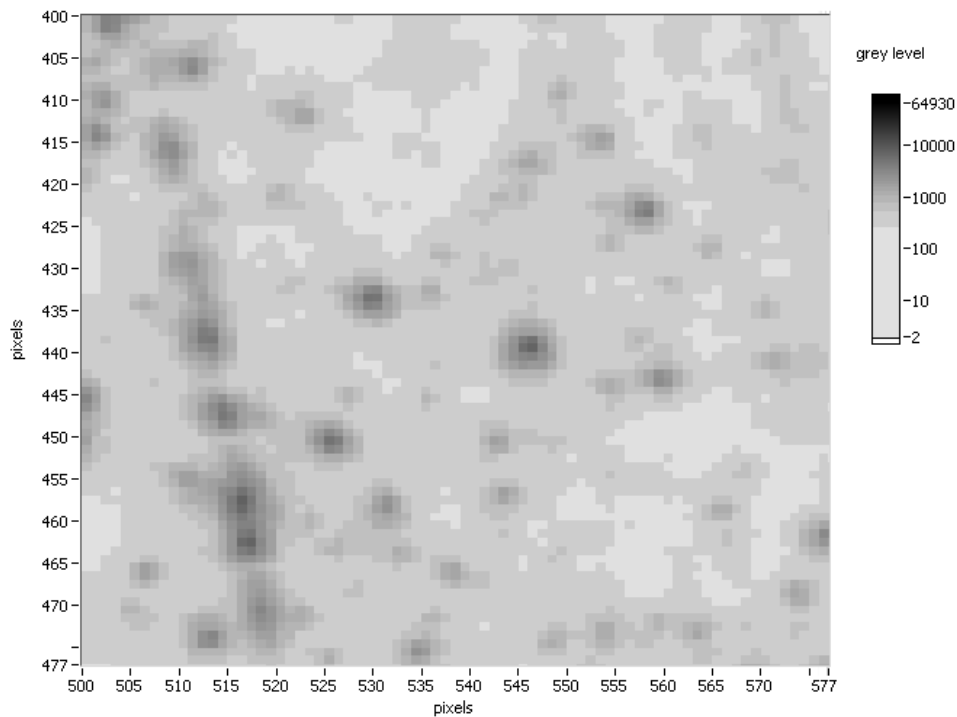


Fig. 17: Enlarged view of the 2 mm square test area. The CCD image recorded for a lighting angle of 13.5° (inverted logarithmic scale).

The displayed surface has typically the dimensions of areas characterized by standard BRDF measurements. In standard configurations, the BRDF recorded would be the global BRDF of this region obtained by averaging over all pixels. It is plotted in Fig. 16. We can see it does not exhibit any oscillations whatsoever. It is also characterized by a scattering level about 5 times higher than the intrinsic response of the surface.

With our CCD-ARS set up, this $2 \times 2 \text{ mm}^2$ region is divided in $77 \times 77 = 5929$ elementary pixels and we acquire the BRDF of each one of these 5929 elementary surfaces. For example, in Fig. 18, we plot the BRDF of two elementary surfaces selected within the global surface displayed Fig. 17, one containing a defect and the other being defect free.

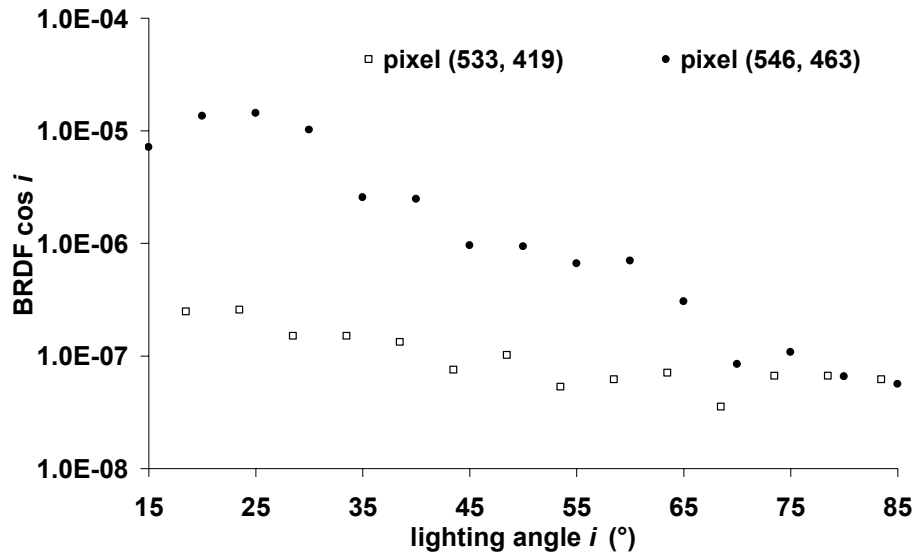


Fig. 18: Cosine-corrected BRDFs of two pixels selected in the area defined Fig. 17, one is defect free and the other shows the presence of a defect

These results are in perfect accordance with the numerical simulations presented in Section 2 (see especially Fig. 3). It also illustrates the kind of erroneous information that can be produced by classical BRDF instruments when the surface topology includes localized defects[15, 19].

4.4 Conclusion and perspectives

This paper has been devoted to the description of the last improvements of the CCD-ARS set up developed at the Institut Fresnel for measuring the scattered light function of a low-roughness surface. The application range of the instrument has been outstandingly improved. First, the angular range has been extended in order to reach angles from 65° to 90° by designing an original lighting system which provides a constant square shaped spot on the sample surface during the whole scan. Furthermore, an atypical sample holder has been achieved and, coupled with the new lighting system, it reduces drastically the parasitic light.

This new instrument can provide comprehensive information on surface defects as well as measuring the correct intrinsic roughness. The number of useful data points acquired during a single scan using this device can easily reach several millions. The positions and sizes of defects can be determined from obvious features of the scattered light profile in each CCD pixel. This apparatus can therefore be used to efficiently compare and qualify optical coating deposition processes.

Now, the experimental set up is operational and each scan gives a huge amount of information. So, to further improve this method, it seems essential to focus our work on the way to compute these data. The complete scan of a sample could lead to the localisation of all the localized defects in presence on the 25 mm diameter sample. These defects would be immediately classified and numerically suppressed from the sample studied. This would permit the achievement of a roughness mapping of the whole sample surface divided in 26 x 26 μm^2 elementary surfaces. We can see here the impressive number of information which can be extracted from only one 20 minutes acquisition performed with our CCD-ARS set up.

Finally, the theoretical principles behind this roughness measurement method are clearly compatible with other spectral studies (wavelength switching of incoherent sources) and polarization analysis, as previously defined by our team on a standard ARS instrument [20-22].

REFERENCES

[1] Bennett, J. M. and Mattson, L., "Introduction to surface roughness and scattering, 2nd Ed," in *OSA*, Washington DC (1999).

- [2] Amra, C., "From light scattering to the microstructure of thin-film multilayers," *Appl. Opt.* 32(28), 5481 (1993)
- [3] Duparré, A. and Kassam, S., "Relation between light scattering and the microstructure of optical thin films," *Appl. Opt.* 32(28), 5475-5480 (1993)
- [4] Amra, C., "Light scattering from multilayer optics. II. Application to experiment," *J. Opt. Soc. Am. A* 11(1), 211 (1994)
- [5] Amra, C., "Light scattering from multilayer optics. I. Tools of investigation," *J. Opt. Soc. Am. A* 11(1), 197 (1994)
- [6] Amra, C., Grezes, B. C., Roche, P. and Pelletier, E., "Description of a scattering apparatus: application to the problems of characterization of opaque surfaces," in *Applied Optics. 15 July 1989; 28(14): 2723-30* (1989).
- [7] Roche, P. and Pelletier, E., "Characterizations of optical surfaces by measurement of scattering distribution," *Appl. Opt.* 23(20), 3561-3566 (1984)
- [8] Germer, T. and Asmail, C., "Goniometric optical scatter instrument for out-of-plane ellipsometry measurements," *Review of Scientific Instruments* 70(9), 3688-3695 (1999)
- [9] Duparre, A., Ferre, B. J., Gliech, S., Notni, G., Steinert, J. and Bennett, J. M., "Surface characterization techniques for determining the root-mean-square roughness and power spectral densities of optical components," *Applied Optics* (2002)
- [10] White, D. R., Saunders, P., Bonsey, S. J., van de Ven, J. and Edgar, H., "Reflectometer for Measuring the Bidirectional Reflectance of Rough Surfaces," *Appl. Opt.* 37(16), 3450-3454 (1998)
- [11] Lequime, M., Zerrad, M., Deumie, C. and Amra, C., "A goniometric light scattering instrument with high-resolution imaging," *submitted to optics communications* (2008)
- [12] Zerrad, M., Lequime, M., Deumie, C. and Amra, C., "Characterization of Optical Coatings with a CCD Angular and Spatial Resolved Scatterometer," in *Optical Interference Coatings*, p. ThA5, Optical Society of America (2007).
- [13] Deumié, C., Richier, R., Dumas, P. and Amra, C., "Multiscale roughness in optical multilayers: atomic force microscopy and light scattering," *Appl. Opt.* 35(28), 5583-5594 (1996)
- [14] Amra, C., Grezes-Besset, C. and Bruel, L., "Comparison of surface and bulk scattering in optical multilayers," *Appl. Opt.* 32(28), 5492 (1993)
- [15] Maure, S., Albrand, G. and Amra, C., "Low-level scattering and localized defects," *Appl. Opt.* 35(28), 5573-5582 (1996)
- [16] <http://www.superlumdiodes.com/pdf/s840-b-i-20.pdf>
- [17] <http://www.piaction.com/products/imcam/pixis/default.aspx>
- [18] <http://www.lw4u.com/super-eye-lens-tables.htm>
- [19] Zerrad, M., Deumié, C., Lequime, M. and Amra, C., "An alternative scattering method to characterize surface roughness from transparent substrates," *Opt. Express* 15(15), 9222-9231 (2007)
- [20] Lequime, M., Abel, L. and Deumié, C., "Colorimetric properties of the light scattered by various objects," in *Proceedings of the SPIE The International Society for Optical Engineering. 25 Feb. 2004; 5250(1): 271-7* (2004).
- [21] Gilbert, O., Deumié, C. and Amra, C., "Angle-resolved ellipsometry of scattering patterns from arbitrary surfaces and bulks," *Opt. Express* 13(7), 2403-2418 (2005)
- [22] Amra, C., Zerrad, M., Siozade, L., Georges, G. and Deumié, C., "Partial polarization of light induced by random defects at surfaces or bulks," *Opt. Express* 16(14), 10372-10383 (2008)